

# Study of hybrid driven micromirrors for 3-D variable optical attenuator applications

Kah How Koh,<sup>1</sup> Bo Woon Soon,<sup>1,2</sup> Julius Minglin Tsai,<sup>2</sup> Aaron J. Danner,<sup>1</sup> and Chengkuo Lee<sup>1,\*</sup>

<sup>1</sup>Department of Electrical & Computer Engineering, National University of Singapore, 4 Engineering Drive 3, Singapore 117576, Singapore

<sup>2</sup>Institute of Microelectronics, A\*STAR (Agency for Science, Technology and Research), 11 Science Park Road, Singapore 117685, Singapore

\*elelc@nus.edu.sg

**Abstract:** Aluminium-coated micromirrors driven by electrothermal and electromagnetic actuations have been demonstrated for 3-D variable optical attenuation applications. Three types of attenuation schemes based on electrothermal, electromagnetic and hybrid, i.e. combination of electrothermal and electromagnetic, actuations have been developed. In addition, two different designs have been fabricated and characterized to investigate the effects of the variations made to both the actuators on the optical attenuation performances of the micromirror. Our unique design of using both ET and EM actuators simultaneously to achieve attenuation is the first demonstration of such hybrid driven CMOS compatible MEMS VOA device.

©2012 Optical Society of America

**OCIS codes:** (230.4685) Optical microelectromechanical devices; (230.4040) Mirrors.

---

## References and links

1. W. Noell, P. A. Clerc, L. Dellmann, B. Guldemann, H. P. Herzig, O. Manzano, C. R. Marxer, K. J. Weible, R. Dandliker, and N. de Rooij, "Applications of SOI-based optical MEMS," *IEEE J. Sel. Top. Quantum Electron.* **8**(1), 148–154 (2002).
2. M. C. Wu, O. Solgaard, and J. E. Ford, "Optical MEMS for lightwave communication," *J. Lightwave Technol.* **24**(12), 4433–4454 (2006).
3. K. H. Koh, T. Kobayashi, F.-L. Hsiao, and C. Lee, "Characterization of piezoelectric PZT beam actuators for driving 2D scanning micromirrors," *Sens. Actuators A Phys.* **162**(2), 336–347 (2010).
4. K. H. Koh, T. Kobayashi, J. Xie, A. Yu, and C. Lee, "Novel piezoelectric actuation mechanism for a gimbal-less mirror in 2D raster scanning applications," *J. Micromech. Microeng.* **21**(7), 075001 (2011).
5. K. H. Koh, T. Kobayashi, and C. Lee, "A 2-D MEMS scanning mirror based on dynamic mixed mode excitation of a piezoelectric PZT thin film s-shaped actuator," *Opt. Express* **19**(15), 13812–13824 (2011).
6. A. D. Aguirre, P. R. Hertz, Y. Chen, J. G. Fujimoto, W. Piyawattanametha, L. Fan, and M. C. Wu, "Two-axis MEMS scanning catheter for ultrahigh resolution three-dimensional and en face imaging," *Opt. Express* **15**(5), 2445–2453 (2007).
7. J. Sun, S. J. Lee, L. Wu, M. Sarntinoranont, and H. Xie, "Refractive index measurement of acute rat brain tissue slices using optical coherence tomography," *Opt. Express* **20**(2), 1084–1095 (2012).
8. C. Lee and J. A. Yeh, "Development and evolution of MOEMS technology in variable optical attenuators," *J. Micro/Nanolith. MEMS MOEMS* **7**, 021003 (2008).
9. H. Toshiyoshi and H. Fujita, "Electrostatic micro torsion mirrors for an optical switch matrix," *J. Microelectromech. Syst.* **5**(4), 231–237 (1996).
10. Y.-J. Yang, B.-T. Liao, and W.-C. Kuo, "A novel 2 × 2 MEMS optical switch using the split cross-bar design," *J. Micromech. Microeng.* **17**(5), 875–882 (2007).
11. A. Q. Liu and X. M. Zhang, "A review of MEMS external-cavity tunable lasers," *J. Micromech. Microeng.* **17**(1), R1–R13 (2007).
12. C. R. Giles, V. Aksyuk, B. Barber, R. Ruel, L. Stulz, and D. Bishop, "A silicon MEMS optical switch attenuator and its use in lightwave subsystems," *IEEE J. Sel. Top. Quantum Electron.* **5**(1), 18–25 (1999).
13. C. Marxer, P. Griss, and N. F. de Rooij, "A variable optical attenuator based on silicon micromechanics," *IEEE Photon. Technol. Lett.* **11**(2), 233–235 (1999).
14. A. Q. Liu, X. M. Zhang, C. Lu, F. Wang, C. Lu, and Z. S. Liu, "Optical and mechanical models for a variable optical attenuator using a micromirror drawbridge," *J. Micromech. Microeng.* **13**(3), 400–411 (2003).
15. C. Lee, Y.-S. Lin, Y.-J. Lai, M. H. Tasi, C. Chen, and C.-Y. Wu, "3-V driven pop-up micromirror for reflecting light toward out-of-plane direction for VOA applications," *IEEE Photon. Technol. Lett.* **16**(4), 1044–1046 (2004).

16. R. R. A. Syms, H. Zou, J. Stagg, and H. Veladi, "Sliding-blade MEMS iris and variable optical attenuator," *J. Micromech. Microeng.* **14**(12), 1700–1710 (2004).
17. H. Cai, X. M. Zhang, C. Lu, A. Q. Liu, and E. H. Khoo, "Linear MEMS variable optical attenuator using reflective elliptical mirror," *IEEE Photon. Technol. Lett.* **17**(2), 402–404 (2005).
18. J. A. Yeh, S.-S. Jiang, and C. Lee, "MOEMS variable optical attenuators using rotary comb drive actuators," *IEEE Photon. Technol. Lett.* **18**(10), 1170–1172 (2006).
19. C. Chen, C. Lee, and J. A. Yeh, "Retro-reflection type MOEMS VOA," *IEEE Photon. Technol. Lett.* **16**(10), 2290–2292 (2004).
20. T.-S. Lim, C.-H. Ji, C.-H. Oh, H. Kwon, Y. Yee, and J. U. Bu, "Electrostatic MEMS variable optical attenuator with rotating folded micromirror," *IEEE J. Sel. Top. Quantum Electron.* **10**(3), 558–562 (2004).
21. C. Lee, "A MEMS VOA Using Electrothermal Actuators," *J. Lightwave Technol.* **25**(2), 490–498 (2007).
22. X. M. Zhang, A. Q. Liu, H. Cai, A. B. Yu, and C. Lu, "Retro-Axial VOA using parabolic mirror pair," *IEEE Photon. Technol. Lett.* **19**(9), 692–694 (2007).
23. N. A. Riza and S. Sumriddetchkajorn, "Digitally controlled fault-tolerant multiwavelength programmable fiber-optic attenuator using a two-dimensional digital micromirror device," *Opt. Lett.* **24**(5), 282–284 (1999).
24. W. Sun, W. Noell, M. Zickar, M. J. Mughal, F. Perez, N. A. Riza, and N. F. de Rooij, "Design, simulation, fabrication, and characterization of a digital variable optical attenuator," *J. Microelectromech. Syst.* **15**(5), 1190–1200 (2006).
25. K. Isamoto, K. Kato, A. Morosawa, C. Chong, H. Fujita, and H. Toshiyoshi, "A 5-V operated MEMS variable optical attenuator by SOI bulk micromachining," *IEEE J. Sel. Top. Quantum Electron.* **10**(3), 570–578 (2004).
26. C. Lee, F.-L. Hsiao, T. Kobayashi, K. H. Koh, P. V. Ramana, W. Xiang, B. Yang, C. W. Tan, and D. Pinjala, "A 1-V operated MEMS variable optical attenuator using piezoelectric PZT thin-film actuators," *IEEE J. Sel. Top. Quantum Electron.* **15**(5), 1529–1536 (2009).
27. K. H. Koh, C. Lee, and T. Kobayashi, "A piezoelectric-driven three-dimensional MEMS VOA using attenuation mechanism with combination of rotational and translational effects," *J. Microelectromech. Syst.* **19**(6), 1370–1379 (2010).
28. H.-T. Hsieh, C.-H. Li, and G.-D. J. Su, "Amorphous fluoropolymer micromembrane for variable optical attenuation," *Sens. Actuators A Phys.* **168**(1), 172–178 (2011).
29. Y. Hongbin, Z. Guangya, C. F. Siang, and L. Feiwen, "A variable optical attenuator based on optofluidic technology," *J. Micromech. Microeng.* **18**(11), 115016 (2008).
30. P. Müller, A. Kloss, P. Liebraut, W. Mönch, and H. Zappe, "A fully integrated optofluidic attenuator," *J. Micromech. Microeng.* **21**(12), 125027 (2011).
31. I. J. Cho, T. Song, S.-H. Baek, and E. Yoon, "A low-voltage and low-power RF MEMS series and shunt switches actuated by combination of electromagnetic and electrostatic forces," *IEEE Trans. Microw. Theory Tech.* **53**(7), 2450–2457 (2005).
32. B. Yang, C. Lee, W. L. Kee, and S. P. Lim, "Hybrid energy harvester based on piezoelectric and electromagnetic mechanisms," *J. Micro/Nanolith. MEMS MOEMS* **9**, 023002 (2010).

## 1. Introduction

Since the early 1990s, research involving the utilization of silicon micromachining technology on micromirrors has attracted a great deal of attention because of their wide range of applications in optical communication [1, 2], 2-D scanning display [3–5], and endoscopic bioimaging [6, 7]. In the late 1990s, the booming telecommunication market stimulated enormous investment in microelectromechanical systems (MEMS) technology as it has been recognized to be the missing link connecting existing technologies to form an all-optical communication network. With advantages of handling optical signals in a way of protocol transparency and of data rate and wavelength independence, MEMS-based solutions have been successfully integrated into various tunable devices in the optical network such as variable optical attenuators (VOAs) [8], optical switches [9, 10] and tunable lasers [11].

VOA is commonly considered to be a key component to groom power levels across the wavelength division multiplexing spectrum, minimizing crosstalk and maintaining the desired signal-to-noise ratio. Most of the designs of MEMS VOAs reported in the literature adopted attenuation schemes that can be generally classified into three groups: shutter-type [12–16], planar reflective-type [17–22] and three-dimensional (3-D) reflective-type [23–27]. Pioneering works of MEMS-based VOAs based on shutter-type designs were first conducted in 1998 by Giles *et al.* [12] and Marxer *et al.* [13]. By using a polysilicon micromirror arranged between the coaxially aligned input and output fibers, the micromirror functions as a shutter when actuated, hence tuning the percentage of light blocked by it. Such attenuation scheme based on the shutter design offers benefits such as low insertion loss and large attenuation range due to the close proximity between the input and output fibers. However, it suffers from strong back reflection due to the coaxial fiber assembly configuration. With a

well optimized deep reactive ion etch (DRIE) process and appropriate selection of lens fiber, planar reflective MEMS VOA designs begin to surface in the early 2000s due to several advantages such as low wavelength dependent loss (WDL) and negligible back reflection. Two commonly adopted designs for planar reflective type include using single-reflective [17, 18] and retro-reflective micromirrors [19–22], while attenuation is achieved as a result of the change in coupling efficiency between the input and output fiber when the micromirror is actuated. To address the layout format concern with the 45° offset between the input and out fiber ports for not being a common layout configuration in application market, planar retro-reflective type VOA designs were introduced to overcome this problem.

Another key approach of making MEMS VOA devices involves the integration of large reflective mirrors with optics typically realized in 3-D free space configuration [23–27]. When such tilt reflective mirrors are deployed for 3-D optical attenuation in conjunction with large micro-optics such as dual fiber collimator, the resulting VOA device can gain excellent data in terms of return loss and WDL under reasonable driving voltage. A 3-D VOA based on DMD mirror array from Texas Instruments has been demonstrated in 1999 [23], while Sun *et al.* deployed a digital VOA using an array of 16 equal-length rectangular micromirrors [24]. Besides using an array of micromirrors to form a multi-bit digital VOA, a large single reflective mirror may also be used for attenuation purpose. In 2004, Isamoto *et al.* have demonstrated a 3-D VOA using electrostatic parallel plate actuation in which the derived performance was outstanding as only 4.5 V<sub>dc</sub> was needed to achieve 40 dB attenuation range [25]. New progress in attenuation mechanism based on optofluidic technology has also been demonstrated on various kinds of polymer based VOA devices [28–30]. For example, an electrostatic actuated polymeric deformable mirror aligned with a dual fiber collimator has been reported, achieving 33 dB attenuation range at 150 V<sub>dc</sub>, 125 μW [28]. In the regime of optofluidic attenuation, Yu *et al.* developed a transmissive type VOA with a pneumatic controllable polymeric membrane [29] while Müller *et al.* demonstrated optical attenuation through the movement of a liquid droplet in and out of the optical path using on-chip electrowetting-on-dielectric (EWOD) actuation [30].

In recent years, 3-D MEMS VOA driven by piezoelectric Pb(Zr,Ti)O<sub>3</sub> (PZT) thin film actuators have been demonstrated in our previous research attempts, achieving 40 dB dynamic attenuation range at 1V<sub>dc</sub> [26, 27]. However, PZT is not a CMOS compatible material. With the future vision of having a monolithic integrated MEMS VOA with CMOS integrated circuits, we endeavor to develop a CMOS compatible actuation design to achieve optical attenuation. Thus, in this paper, we explore novel, CMOS compatible, 3-D MEMS VOA that can be operated by either electrothermal (ET) or electromagnetic (EM) actuation. These two actuation mechanisms are primarily considered due to their low driving voltage and CMOS compatibility, hence allowing for lower fabrication cost and ease of integration with CMOS transistor circuit which allows a MEMS VOA device with electronic feedback to be developed in the future. In addition, hybrid actuation, i.e. combination of both EM and ET actuations, can be obtained by addressing voltage biases to both the actuators simultaneously. Our approach of hybrid actuation differs greatly from those planar and 3-D VOA designs that have already been reported in literature, where only one form of actuation was used to drive the micromirror or shutter. The advantages in utilizing hybrid actuation mechanism have already been demonstrated in various kinds of MEMS devices such as RF switches [31] and energy harvesters [32]. The combination of both electromagnetic and electrostatic actuation mechanisms in the RF switch design proposed by Cho *et al.* allows them to achieve excellent switching characteristics at low power and voltage [31]. Similarly, for the case of energy scavenging, the harvester demonstrated higher output power density when both the piezoelectric and electromagnetic elements are used [32]. Experimental study of both actuation mechanisms, along with hybrid actuation, will be described, while comparison in attenuation performance among the two fabricated VOA devices of different ET and EM actuator designs are also made.

## 2. Design and modeling

### 2.1 Actuation mechanisms and attenuation principles

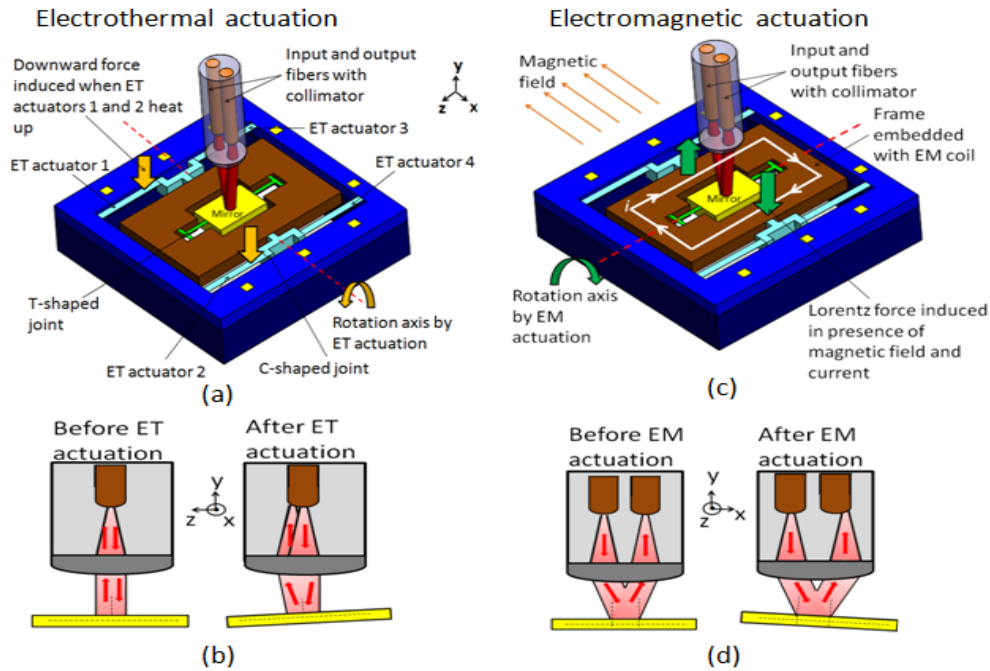


Fig. 1. (a) Schematic diagram showing the (a) ET actuation mechanism where ET actuators 1 and 2 are biased and heated up, (b) ET attenuation principle, (c) EM actuation mechanism in the presence of an external permanent magnetic field and current flowing in the coils embedded in the frame, and (d) EM attenuation principle.

Schematic diagrams showing the proposed hybrid 3-D MEMS VOA and the working principles of the actuation mechanisms are illustrated in Figs. 1(a)-(d). The micromirror, which is connected to the outer frame by T-shaped joint, is deposited with a layer of aluminium (Al) on its surface. A dual fiber collimator is arranged in a 3-D free space configuration in which the infra-red (IR) laser beam is focused on the center of the mirror. The rotation axes, which are driven by ET and EM actuations, are designed to be orthogonal to each other such that the mirror is able to move with six degrees of freedom for 3-D attenuation arrangement. When the actuators are initially unbiased, the mirror surface is aligned perpendicular to the dual fiber collimator, causing the entire laser beam to be reflected from the input fiber to the output fiber and resulting in negligible optical attenuation.

Figure 1(a) shows the ET actuation mechanism of the VOA device, where four ET bimorph actuators, numbered 1-4, are designed along the longitudinal sides of the mirror. The ET actuators, which are made of silicon (Si) cantilever fabricated from the device layer of a silicon-on-insulator (SOI) wafer and Al deposited and patterned on it, are anchored to the substrate and attached to the outer frame by rigid and thick C-shaped joints. A thin layer of silicon dioxide is deposited to provide thermal insulation from the ambient environment. When the ET actuators are biased, the differential expansion of Si and Al due to joule heating effect will cause the actuators to bend downward in the negative y-direction. To introduce a mechanical torque about the x-axis, both ET actuators 1 and 2 or 3 and 4 are to be biased serially so that either set of actuators will experience downward displacement simultaneously. This introduces a mechanical rotation angle to the micromirror plate as shown in Fig. 1(b), causing the reflected laser beam to be displaced away from the output fiber and resulting in attenuation.

In the case for EM actuation, the frame is embedded with numerous turns of Al EM coils fabricated in two layers. Both layers of coils run in the same clockwise direction so that the Lorentz forces generated in both layers are the same. As shown in Fig. 1(c), a pair of permanent magnets is arranged such that a uniform magnetic field along the x-direction is formed across the device. When the EM coils are biased and a current flows in a clockwise direction, a pair of equal but opposite Lorentz force will be generated at the coils orthogonal to the magnetic field, causing the micromirror to rotate about the z-axis. This causes a portion of the laser beam to no longer couple into the output fiber as illustrated in Fig. 1(d), resulting in attenuation.

## 2.2 ET actuation design and consideration

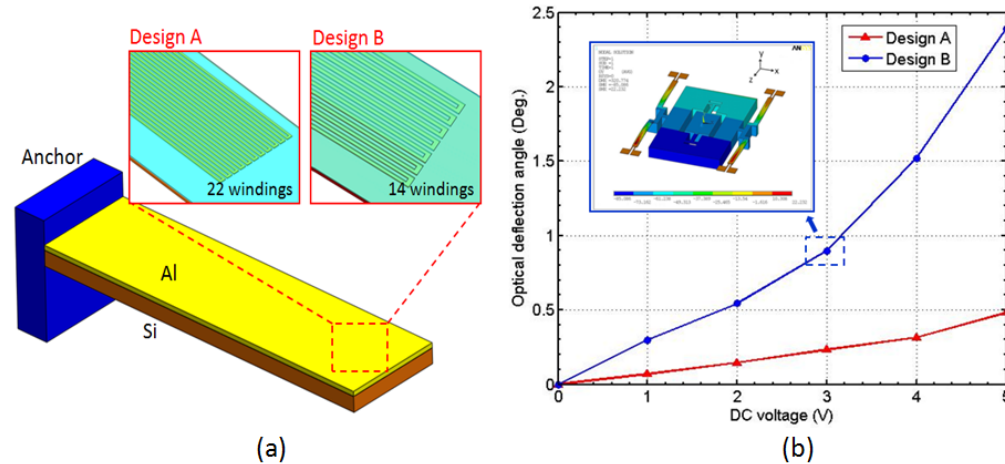


Fig. 2. (a) Schematic diagram illustrating the proposed ET bimorph actuator for two designs A and B. (b) Simulated plot of optical deflection angle versus dc voltage applied to ET actuators 1 and 2. Results are obtained from ANSYS simulation software.

Two designs of the hybrid MEMS VOA have been developed in this research attempt to investigate the effect of both ET and EM actuations on the attenuation performance of the two designs i.e. designs A and B. Instead of using a rectangular piece of Al as the layout design for the material for higher coefficient of expansion, a meandering layout in the form of windings is being considered. Such a winding design will increase the electrical and thermal resistance of the ET actuator, hence reducing chances of actuator burnout and increasing its reliability. When a bias is applied and current flows through the windings, the Al windings heat up and expand more than Si, causing the ET actuator to bend downwards.

As shown in Fig. 2(a), two designs of the ET bimorph actuators have been considered. In design A, 22 Al windings are being fabricated on the Si cantilever while in design B, only 14 Al windings are made. Finite element method (FEM) based on both the ET actuator designs have been made using ANSYS simulation software. Table 1 summarizes the thermo-mechanical properties of the materials used during the simulation. The simulated plots of optical deflection angle versus total dc voltage applied to actuators 1 and 2 for both designs are shown in Fig. 2(b). From Fig. 2(b), it can be observed that the optical deflection angle of the micromirror increases with applied dc voltage. This is expected as increase dc voltage will result in larger current flow and heating effect of the ET actuator. From our previous experiences of VOA characterization in refs [26, 27], it is noted that only optical deflection angle of less than  $0.6^\circ$  is needed for 40 dB attenuation. Based on simulation results, this means that both our ET actuator designs satisfy the criteria for VOA application. In addition, for the same applied dc voltage, design B performs better than design A as the micromirror undergoes a greater rotation angle in the former design. This is due to the lower number of windings in design B compared to design A, hence allowing the ET actuator for design B to

have better electrical and thermal conductivity. To prevent thermal runaway and burnout of the ET actuator for design B, the maximum temperature of the device was also extracted during the simulation. At 4 V<sub>dc</sub>, a maximum simulated temperature of 170 °C is obtained, which is well below the melting point of Al at 660 °C. This signifies good device reliability within the bias range of 4 V<sub>dc</sub> for design B. In addition, modal analysis based on finite element software has also been done to investigate the mechanical resonant frequency of the device. Calculated eigenfrequencies of 84 Hz and 152 Hz are obtained, which correspond to the vertical and horizontal tilting caused by ET and EM actuations, respectively. This makes our device rather stable when subjected to ambient vibrations usually in the range of few tens of Hz, while offering low spring constant for larger optical deflection angle.

**Table 1. Thermo-mechanical Properties of Materials used for ET Actuator Simulation in ANSYS**

Thin film materials	Density (kgm <sup>-3</sup> )	Young's Modulus (10 <sup>9</sup> Pa)	Poisson ratio	Thermal conductivity (Wm <sup>-1</sup> K <sup>-1</sup> )	Coefficient of thermal expansion (10 <sup>-6</sup> K <sup>-1</sup> )	Resistivity (10 <sup>-3</sup> Ωm)
Al	2700	65	0.33	237	23.1	2.82 × 10 <sup>-5</sup>
SiO <sub>2</sub>	2200	74	0.17	1.04	0.4	1 × 10 <sup>19</sup>
Si	2330	162	0.28	150	2.6	100

### 2.3 EM actuation design and consideration

Similar to ET actuation, two designs of EM actuation have also been considered. The out-of-plane Lorentz force acting on a dc carrying conductor is given as:

$$F = \oint_L Idl \times B \quad (1)$$

where  $I$  is the current flowing in a close loop wire of length  $L$  and  $B$  is the external permanent magnetic field. When a current flows in the EM coils embedded in the outer frame, the pair of Lorentz force introduces a magnetic torque and causes the micromirror to rotate about the z-axis. The torque generated about z-axis by the two layers of EM coils may be approximated as:

$$T = iB \sum_{m=0}^{N-1} (b + 2m \cdot \Delta L)(a + 2m \cdot \Delta L) \quad (2)$$

where  $i$  is the current flowing in the EM coils,  $N$  is the number of coil turns,  $a$  and  $b$  are the side lengths of the most inner coil turn on the short and long sides of the frame respectively,  $\Delta L$  is the pitch of the EM coil. The first term in the summation component of (2) arises from the Lorentz force generated due to the current carrying coils that are parallel to the z-axis while the second term arises from the torque induced from the Lorentz force generated in all the coils. Thus, from (2), it can be interpreted that a larger current flowing in the EM coil will generate a larger torque and mechanical rotation of the micromirror. With this consideration, two EM coil designs of different electrical resistances have been proposed, with design B having a lower EM coil resistance compared to design A. Both the dimensions and layout of the EM coil for the two designs are kept the same except for the electrical connection type between the two layers of EM coil. In design A, both layers of the EM coils are connected in series, whereas in design B, both the layers of the EM coils are connected in parallel. The parallel connection between the EM coils in design B allows the effective resultant electrical resistance of the two layers of EM coils to be lowered, hence allowing a larger current to flow in it.

### 3. Device microfabrication

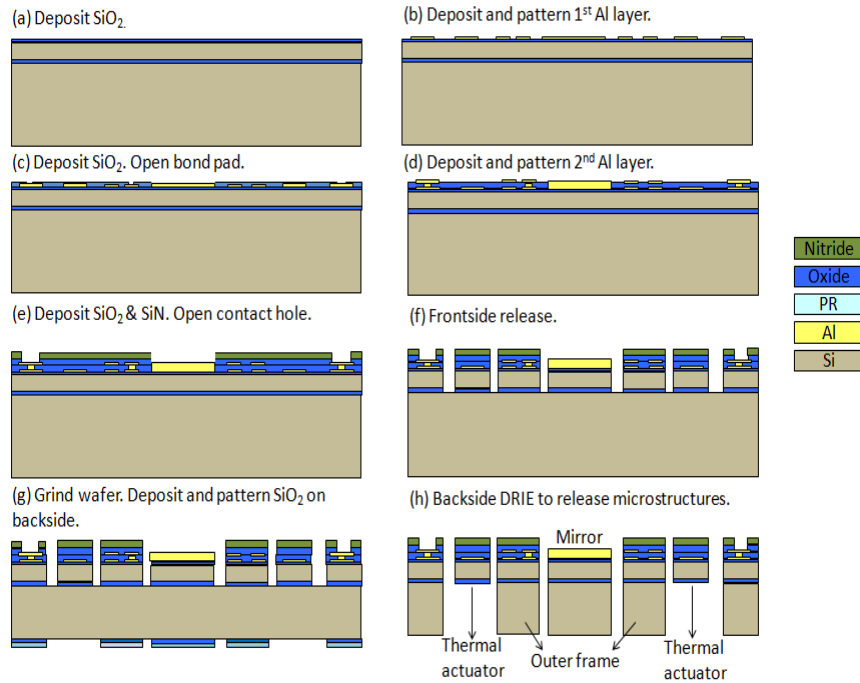


Fig. 3. Microfabrication process flow of the VOA device.

Figure 3 shows the CMOS compatible microfabrication process flow of the hybrid MEMS VOA device reported in this paper. An 8 inch SOI wafer with 3  $\mu\text{m}$  thick Si device layer, 1.1  $\mu\text{m}$  thick buried oxide (BOX) layer and 725  $\mu\text{m}$  Si handle layer was used as the starting material. First, a 0.2  $\mu\text{m}$  thick thermal insulating  $\text{SiO}_2$  was deposited on the front side of the wafer by plasma-enhanced chemical vapor deposition (PECVD) [see Fig. 3(a)]. Next, physical vapor deposition (PVD), patterning and reactive ion etching (RIE) of 2  $\mu\text{m}$  thick Al were done at regions such as the ET actuator windings, EM coils, bond pad and mirror regions [see Fig. 3(b)]. A 0.5  $\mu\text{m}$  thick  $\text{SiO}_2$ , which serves as thermal and electrical insulation for the ET windings and EM coil regions, respectively, was next deposited by PECVD. The bond pads were then opened by RIE of  $\text{SiO}_2$  using  $\text{CHF}_3$  [see Fig. 3(c)]. A second layer of Al was again deposited, patterned and etched, except that the processes this time happen only at the EM coil, mirror and bond pad regions [see Fig. 3(d)]. PECVD  $\text{SiO}_2$  and  $\text{Si}_3\text{N}_4$ , each of 0.5  $\mu\text{m}$  thick, were then deposited as passivating layers. This was followed closely by RIE of  $\text{SiO}_2$  and  $\text{Si}_3\text{N}_4$  contact hole opening. Al remains as the top layer in the mirror region so as to enhance the reflectivity of IR light impinged on the mirror surface [see Fig. 3(e)]. The microstructures such as the ET actuators, C-shaped joints, T-shaped joint and micromirror were then defined from the frontside through RIE of  $\text{Si}_3\text{N}_4$ ,  $\text{SiO}_2$ , Si device and BOX layers using  $\text{CF}_4$  (for  $\text{Si}_3\text{N}_4$ ),  $\text{CHF}_3$  (for  $\text{SiO}_2$ ) and  $\text{SF}_6$  (for Si), respectively [see Fig. 3(f)].

After all the front side wafer processes were finished, the Si handle layer was reduced to 450  $\mu\text{m}$  through backside grinding and polishing. This was followed by backside deposition and patterning of 2  $\mu\text{m}$  thick PECVD  $\text{SiO}_2$ . The photoresist that was used to pattern the  $\text{SiO}_2$  layer remains behind at the backside of the wafer so that both the photoresist and  $\text{SiO}_2$  can act as hard mask material for the subsequent DRIE step [see Fig. 3(g)]. Prior to the DRIE process, the wafer was first diced to the single mirror chip level (6 mm  $\times$  6 mm). The diced mirror chips are then placed on a support wafer and immobilized with adhesive thermal tape. A coarse DRIE step was first done by removing approximately 400  $\mu\text{m}$  thick Si handle layer.

This was followed by several fine DRIE steps of five minutes each so as to gradually remove the remaining 50  $\mu\text{m}$  of Si handle layer. A 450  $\mu\text{m}$  thick Si substrate remains beneath the mirror to maintain the rigidity of it [see Fig. 3(h)].

Figure 4(a) shows the photograph of one of the completed MEMS VOA device packaged in a dual inline package (DIP). The Al bond pads are connected by gold bond wires to the metal pins of the DIP for external biasing. Figures 4(b) and 4(c) illustrate the optical micrographs of the Al windings of the ET actuator for design A (22 windings) and B (14 windings), respectively, while Fig. 4(d) shows the top layer of the EM coil embedded in the outer frame. Figure 4(e) shows the scanning electron microscope photo of the device, which includes the ET actuator, C-shaped joint, frame, T-shaped joint and micromirror. Details of the structural parameters for both designs are summarized in Table 2.

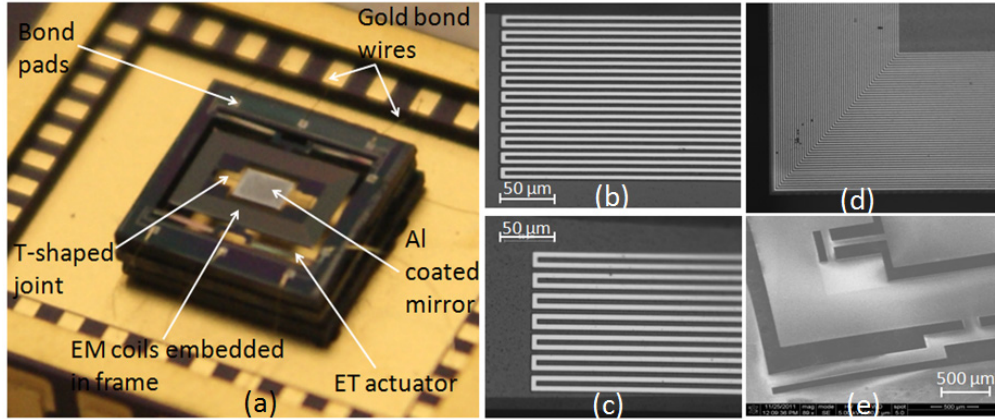


Fig. 4. (a) Photo showing the VOA device packaged in a dual inline package. Optical micrographs showing the (b) Al windings of the ET actuator for design A, (c) Al windings of the ET actuator for design B, and (d) EM coils embedded in the frame. (e) SEM photo illustrating the various microstructures of the VOA device for design B.

**Table 2. Structural Parameters of the Two MEMS VOA Designs**

Structural parameters	Design A	Design B
Die size	6 mm $\times$ 6 mm	
Mirror size (l $\times$ w $\times$ t)	1.5 mm $\times$ 1 mm $\times$ 0.45 mm	
T-shaped joint (w $\times$ t)	150 $\mu\text{m}$ $\times$ 5 $\mu\text{m}$	
ET actuator (l $\times$ w $\times$ t)	1850 $\mu\text{m}$ $\times$ 200 $\mu\text{m}$ $\times$ 7 $\mu\text{m}$	
EM coil (w $\times$ t)	3 $\mu\text{m}$ $\times$ 2 $\mu\text{m}$	
No. of coils in each layer	54	
ET actuator winding (l $\times$ w $\times$ t)	1800 $\mu\text{m}$ $\times$ 3 $\mu\text{m}$ $\times$ 2 $\mu\text{m}$	1800 $\mu\text{m}$ $\times$ 5 $\mu\text{m}$ $\times$ 2 $\mu\text{m}$
No. of ET windings	22	14
Electrical connection type between two layers of EM coils	Series	Parallel

## 4. Device characterization

### 4.1 Experimental setup

The schematic diagram of the MEMS VOA characterization measurement setup is illustrated in Fig. 5(a). The optical measurement setup consists of a tunable IR laser source integrated with a power meter (Agilent 8164B Lightwave Measurement System), two sets of multi-axis X-Y-Z- $\theta_x$ - $\theta_z$  precision alignment stages, dual fiber with collimator and two dc power supplies. The VOA device was mounted on a L-shaped stand attached to one of the adjustable

stage while the dual fiber with collimator was mounted on the second adjustable stage via a fiber holder. The input IR light from the tunable laser was launched via one fiber i.e. input fiber of the dual fiber through the collimator to the center of the mirror. The reflected light was collected by the same collimator to the power meter via the output fiber of the dual fiber. For the initial insertion loss measurement, the relative position of the collimator and mirror was adjusted such that the coupling loss is optimized or minimized. During the fine alignment step, the relative position of the mirror to the collimator was adjusted by moving and tilting both the X-Y-Z- $\theta_x$ - $\theta_z$  stages such that minimum insertion loss is obtained. The  $\theta_x$  and  $\theta_z$  adjustment knobs enable the stage to be tilted with regards to the x- and z-axis respectively. The measured insertion loss in this setup is about 1.8 dB, which is about a decibel higher than commercial VOA products. This is mainly caused by the surface warpage of the mirror and the inferior reflectivity of the Al coating compared to gold at 1550 nm. The whole measurement setup is established on an anti-vibration optical table to reduce the effect of ambient shock to the characterization setup.

Figure 5(b) shows a magnified photo of the device under test (DUT) region, where the DUT is mounted upright in the presence of a permanent magnetic field generated by a pair of Alcomax III magnets, which composed mainly of iron, aluminium, nickel and cobalt. The magnetic field strength at the center of the magnetic field is measured by a Gauss meter to be approximately 0.15 T. The dual fiber collimator is placed at a working distance of 1 mm away from the mirror surface.

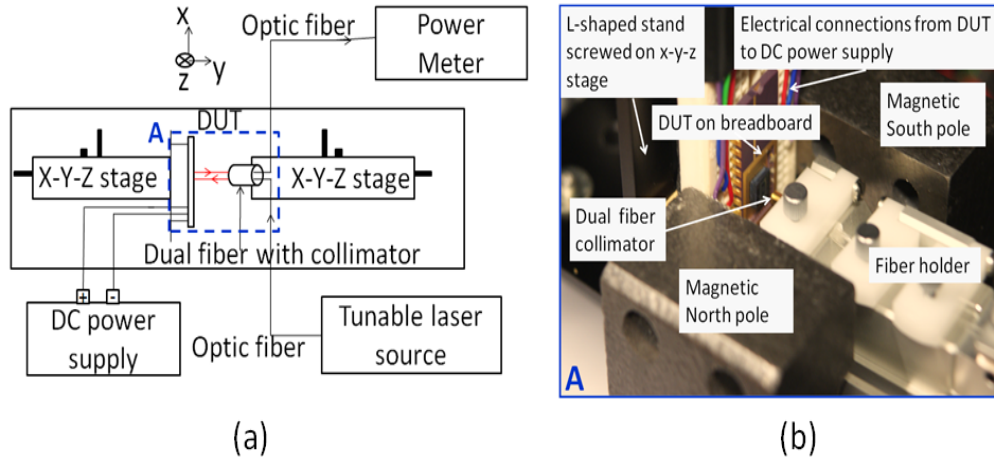


Fig. 5. (a) Schematic diagram of the optical measurement setup conducted on an anti-vibration optical bench. (b) A zoom-in view of the DUT region where the dual fiber collimator is aligned perpendicular to the mirror surface before applying bias to the actuators.

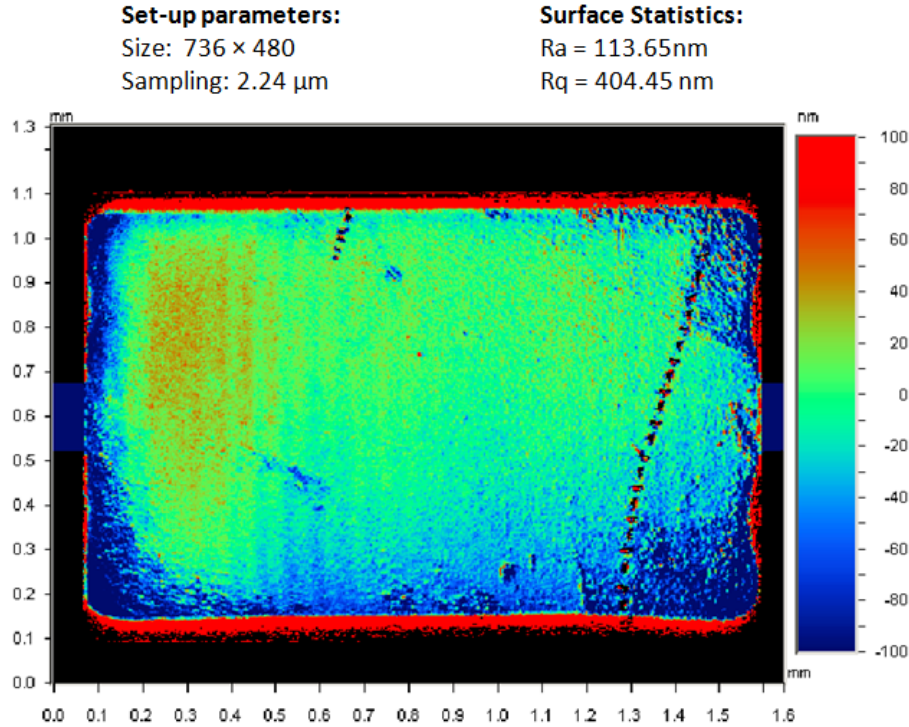


Fig. 6. White light interferometer measurement of the surface roughness for the aluminum coated mirror.

The surface roughness of the fabricated Al-coated mirror measured by Veeco Wyko NT3300 white light interferometer is shown in Fig. 6. The average surface roughness and root mean square roughness are 114nm and 404nm, respectively. The roughness of the mirror surface causes the measured insertion loss to be a decibel higher than commercial available VOA products. Further optimization of the VOA fabrication may improve the surface roughness of the mirror and reduce the insertion loss to less than 1 dB. For example, a very thin layer of sacrificial oxide may first be deposited on top of the aluminium reflective surface in step (e) of the fabrication so that any physical damage sustained during the subsequent steps is on the sacrificial oxide layer. This thin layer of sacrificial oxide can then be etched away using vapour hydrofluoric acid once the microstructures are released from the backside. To further improve the surface quality of the mirror, atomic layer deposition (ALD) of aluminium on the mirror plate, instead of PVD, may also be considered to improve the surface roughness and uniformity of the mirror.

#### 4.2 Experimental results

The I-V curves of the ET windings and EM coils for both designs are shown in Fig. 7(a) and (b), respectively. An Agilent b1500a semiconductor device analyzer was used to bias and obtain the I-V characteristics of both designs. Both ET actuators 1 and 2 were electrically connected in series for the static and attenuation characterizations. This also applies to ET actuators 3 and 4. As observed from Fig. 7(a), for the same applied dc voltage, a larger current is obtained for the ET actuators of design B compared to design A. This is due to a smaller number of Al windings for design B compared to design A, which constitutes to a lower electrical resistance. In ET actuation, the thermal power consumption plays a major role in the actuator performance as the joule heating effect due to the current flow will result in the expansion mismatch between the two materials of the bimorph actuator. In addition, the

I-V curves for the two sets of ET actuators in each of the design are almost identical, with the slight discrepancies due to fabrication process variations.

In the case of EM actuation, the magnitude of the current plays a more pivotal role in the actuation performance compared to that of thermal power consumption for ET actuation. As shown in Fig. 7(b), a larger current is obtained for the EM coils of design B compared to design A for the same applied dc voltage. This is due to the layout design variation made in the two layers of EM coils where series and parallel electrical connections were designed for designs A and B, respectively. In both actuation cases, the I-V curves become non-linear at large applied dc voltage. This is due to the localized heating of the ET windings and EM coils, causing their electrical resistance to increase at high applied voltages.

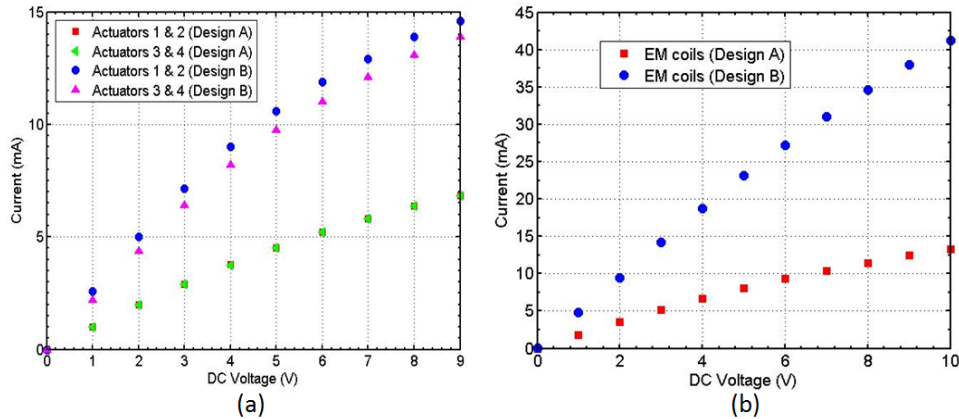


Fig. 7. Measured I-V curves of (a) ET actuators, and (b) EM coils for designs A and B.

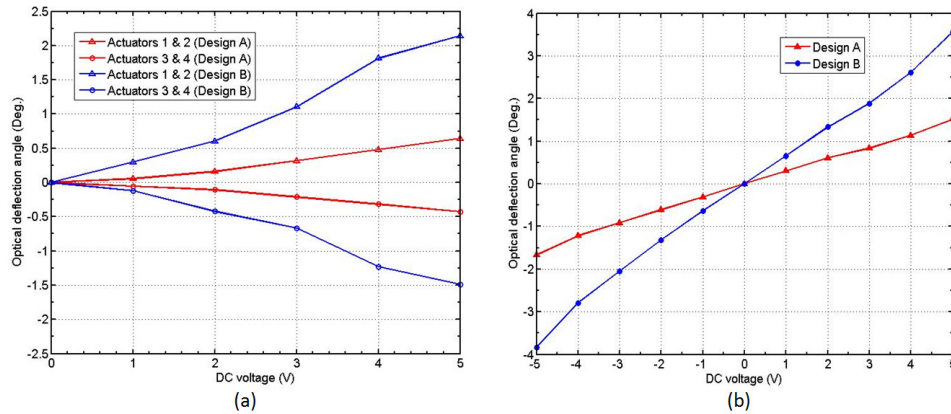


Fig. 8. Measured dc response during (a) ET actuation, and (b) EM actuation for designs A and B.

Figures 8(a) and (b) show the static dc response for ET and EM actuations, respectively. The experiment was carried out using the optical measurement setup involving a red He/Ne laser where it was shone onto the micromirror surface and the displacements of the red laser spot on the screen when different dc voltages applied to the actuators were measured. Details of the He/Ne red laser experimental setups can be found in refs [3–5]. In ET actuation, the static optical deflection angle (ODA) measurement is taken by applying a dc voltage to only one set of serially connected actuators, while leaving the other set unbiased. As shown in Fig. 8(a), when the ET actuators 1 and 2 are biased at  $5V_{dc}$ , the actuators bend down and cause the frame and mirror plate to rotate about the x-axis. This introduces static ODAs of  $+0.6^\circ$  and  $+2.1^\circ$  for designs A and B, respectively. Similarly, when ET actuators 3 and 4 are biased at

$5V_{dc}$ , the frame and mirror rotate in the opposite direction about the same axis, introducing static ODAs of  $-0.4^\circ$  and  $-1.5^\circ$  for designs A and B, respectively. In both cases, the ET actuators for design B perform better than design A. This is due to the lower electrical resistance of the ET actuators in design B compared to design A, hence resulting in larger joule heating effect for the ET actuators in design B. In addition, the dc responses for the two sets of ET actuators in each of the design are almost symmetrical to each other, with the slight discrepancies due to process variations during the fabrication of the ET actuators.

Figure 8(b) shows the dc response for the EM actuation, where positive and negative dc voltages are applied to the EM coils. When a positive bias is applied, the current flows in a clockwise direction around the coils, and the frame experiences a mechanical torque in the presence of a magnetic field. At  $5V_{dc}$ , the mirror rotates about the z-axis, causing an ODA of  $+1.5^\circ$  and  $+2.6^\circ$  for designs A and B, respectively. In the case where negative dc bias is applied, the current flowing in the coil changes direction, i.e. anticlockwise direction. The mirror rotates in the opposite direction about the same axis, introducing an ODA of  $-1.6^\circ$  and  $-3.5^\circ$  for designs A and B, respectively. Similarly for EM actuation, a lower effective EM coil resistance allows a larger current to flow in the coils of design B compared to design A, hence resulting in larger magnetic torque induced in design B.

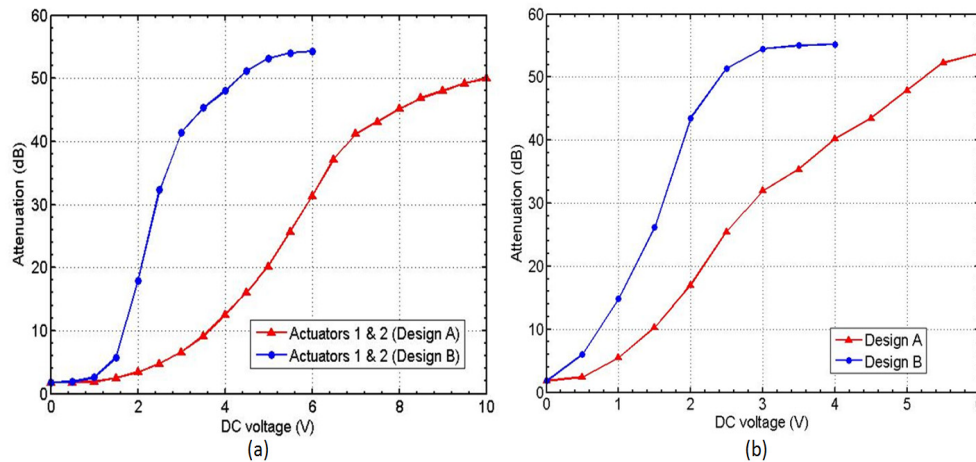


Fig. 9. Measured attenuation-bias response during (a) ET actuation, and (b) EM actuation for designs A and B.

Based on the VOA characterization setup shown previously in Fig. 5, the measured attenuation curves versus dc voltages applied to the ET actuators are demonstrated in Fig. 9(a). The experiment was carried out at a fixed laser wavelength of 1550 nm, with designs A and B obtaining 40 dB dynamic attenuation ranges at  $6.8V_{dc}$  (40 mW) and  $3V_{dc}$  (21 mW), respectively. A 40 dB dynamic attenuation range is sufficient with regards to most of the commercial applications. The ET attenuation scheme for design B again performs better than design A as a lower dc driving voltage is required in the former design for the same attenuation range. In the case of EM attenuation scheme depicted in Fig. 9(b), 40 dB attenuation ranges are achieved at  $4V_{dc}$  (26 mW) and  $1.9V_{dc}$  (18 mW) for designs A and B, respectively. As expected, the EM attenuation scheme for design B outperforms design A in terms of lower driving voltage and power consumption.

The attenuation dependence on wavelengths ranging from 1510 nm to 1610 nm are also measured for both designs at various attenuation states. The wavelength dependence losses for both designs, which are summarized in Table 3, are at similar values with those VOAs already reported in literature. Table 3 also summarizes and compares the performance obtained for design A and B during ET and EM attenuation schemes. Based on Table 3, it is evident that design B performs better than design A in terms of dynamic attenuation range at lower driving voltage and power consumption. Further optimization may be made to both ET

and EM attenuation schemes such that both the electrical resistances of the ET actuator windings and the EM coils can be reduced more. However, care must be taken to prevent the ET actuator and EM coil from experiencing thermal runaway, causing them to be burnt out. Optimization in terms of reduction of driving voltage is the next step to consider so as to further improve the performance of our MEMS VOA devices. The thickness of the bulk silicon beneath the mirror plate and the outer frame may be further reduced so as to decrease the mass inertia, which in turn decreases the response time and operating voltage of the device. More EM coils may be fabricated to increase the magnetic torque contribution at a lower voltage.

**Table 3. VOA Performance of the Two Fabricated Designs**

Specifications	ET attenuation scheme		EM attenuation scheme	
	Design A	Design B	Design A	Design B
Insertion loss	1.8 dB	1.8 dB	1.8 dB	1.8 dB
Dynamic attenuation range	> 50 dB	> 50 dB	> 50 dB	> 50 dB
Wavelength dependent loss	0.5 dB @ 10 dB, 0.6 dB @ 20 dB, 0.4 dB @ 30 dB.	0.3 dB @ 10 dB, 0.5 dB @ 20 dB, 0.4 dB @ 30 dB.	0.3dB @ 10dB, 0.4 dB @ 20dB, 0.5 dB @ 30 dB.	0.2 dB @ 10 dB, 0.4 dB @ 20 dB, 0.5 dB @ 30 dB.
Voltage required for 40dB attenuation range	6.8 V	3 V	4 V	1.9 V
Power consumption	40 mW	21 mW	26 mW	18 mW

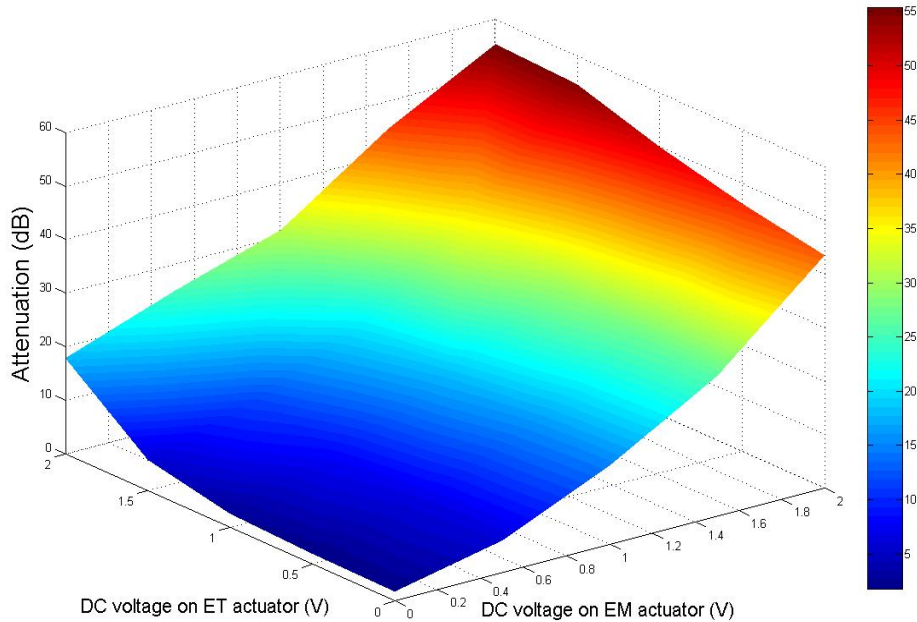


Fig. 10. Measured attenuation-bias response curve during hybrid attenuation scheme for design B where both ET and EM actuators are biased simultaneously.

Besides ET and EM attenuation schemes, hybrid attenuation, i.e. combination of both ET and EM actuations, is also investigated. In hybrid attenuation scheme, dc voltages are applied to the ET and EM actuators simultaneously. Figure 10 shows various dc voltage combinations being applied to the two different actuators of design B while an attenuation characteristic topography is derived. A larger attenuation will be observed when both EM and ET actuators

are biased simultaneously compared to biasing each of them individually. This is because when both orthogonal rotation axes are driven simultaneously, the micromirror will be displaced at an angle to the scanning axes, hence causing the laser beam to be displaced further and achieving a larger optical attenuation. From the attenuation topography, various voltage combinations can be made to both the actuators so as to obtain a 40 dB dynamic attenuation range. For example, when  $1.5 V_{dc}$  are applied to both the ET and EM actuators simultaneously, an attenuation of approximately 40 dB can be obtained. This is equivalent to a total electrical power consumption of 16.2 mW, which is a few mW lower than that achieved by EM attenuation scheme alone at  $1.9 V_{dc}$  by device B. As such, with the hybrid attenuation scheme, lower electrical power consumption and an additional degree of freedom in attenuation control can be attained. More specifically, any deviation of attenuation-DC bias characteristics among the various VOA devices due to fabrication process and assembly steps can be compensated by changing the voltage combinations to the ET and EM actuators. For example, EM actuation can be adopted as the primary attenuation scheme due to its higher efficiency, while ET actuation is used to compensate any small deviations among the various VOA devices that may arise due to fabrication process and assembly steps.

## 5. Conclusion

Novel CMOS compatible MEMS VOAs driven by ET or/and EM actuations have been developed and characterized in a 3-D free space configuration. Both ET and EM actuations have been integrated in the same device for optical attenuation applications. This makes our device essentially different from most of the shutter type, planar reflective and 3-D reflective VOAs that have already been reported in literature where only one actuation mechanism is used to drive the shutter or mirror. In addition, two different designs have been made to investigate the effects of the number of ET actuator windings and the electrical connection type between the two layers of EM coils on the attenuation performances of the VOAs. Design B, which is driven by ET actuator windings and EM coils of lower electrical resistance, performs better than design A, achieving dynamic attenuation ranges of 40 dB at  $3V_{dc}$  and  $1.9V_{dc}$  by ET and EM attenuation schemes, respectively. Wavelength dependent losses have also been demonstrated to be less than 0.6 dB at all attenuation states for both designs. Hybrid attenuation scheme has also been demonstrated successfully, allowing our unique design to consume even lower electrical power i.e. 16.2 mW, and attain an additional degree of freedom in attenuation control.

## Acknowledgments

The authors would like to acknowledge the support by the National University of Singapore under Grant No. R-263-000-598-112, SERC Grant Nos. 0921010049, 1021650084 and 1021010022 from A\*STAR, Singapore, and the Ph.D scholarship grant received from GlobalFoundries Singapore.